Biomech Model Mechanobiol (2010) 9:597–611
DOI 10.1007/s10237-010-0200-3

ORIGINAL PAPER

A nonlocal constitutive model for trabecular bone softening in compression

Mathieu Charlebois · Milan Jirásek · Philippe K. Zysset

Received: 16 May 2009 / Accepted: 15 February 2010 / Published online: 18 March 2010

Abstract Using the three-dimensional morphological data provided by computed tomography, finite element (FE) models can be generated and used to compute the stiffness and strength of whole bones. Three-dimensional constitutive laws capturing the main features of bone mechanical behavior can be developed and implemented into FE software to enable simulations on complex bone structures. For this purpose, a constitutive law is proposed, which captures the compressive behavior of trabecular bone as a porous material with accumulation of irreversible strain and loss of stiffness beyond its yield point and softening beyond its ultimate point. To account for these features, a constitutive law based on damage coupled with hardening anisotropic elastoplasticity is formulated using density and fabric-based tensors. To prevent mesh dependence of the solution, a nonlocal averaging technique is adopted. The law has been implemented into a FE software and some simple simulations are first presented to illustrate its behavior. Finally, examples dealing with compression of vertebral bodies clearly show the impact of softening on the localization of the inelastic process.

Keywords Trabecular bone · Constitutive law · Softening · Nonlocal · Damage · Plasticity · Anisotropy · Fabric

M. Charlebois (✉) · M. Jirásek
Department of Mechanics, Faculty of Civil Engineering,
Czech Technical University in Prague, Thákurova 7,
166 29 Prague, Czech Republic
e-mail: mathieu@ilsb.tuwien.ac.at

P. K. Zysset
Institute of Lightweight Design and Structural Biomechanics,
Vienna University of Technology, Gusshausstrasse 27-29,
1040 Vienna, Austria

1 Introduction

The field of bone mechanics relies on numerical methods, such as the finite element method, to investigate, for example, implant design and predict the stiffness and strength of whole bones (Prendergast 1997; Cristofolini et al. 2007). Three-dimensional bone images obtained from computed tomography provide input for patient-specific numerical models that can be used in clinical studies and treatment evaluation (e.g. Crawford et al. 2003; Melton et al. 2007; Keaveny et al. 2007; Chevalier et al. 2008b). Incorporated in the FE method is the constitutive law, which defines the relation between stresses and strains. Most studies have used simple constitutive relations, for example linear elasticity with isotropic or transverse isotropic symmetry.

So far, only little effort has been devoted to the development of inelastic constitutive models specific to bone (Zysset and Curnier 1996; Fondrk et al. 1999a; Garcia et al. 2009; Natali et al. 2008b). The model presented by Fondrk et al. (1999a) and Natali et al. (2008b) focused on the rate-dependent behavior of compact bone under tension. While the model of Fondrk et al. (1999a) was solely one-dimensional, unsuitable for three-dimensional finite element simulations, the model of Natali et al. (2008b) was implemented and used in dental implant studies (Natali et al. 2008a). The models of Zysset and Curnier (1996) and Garcia et al. (2009) aimed at describing the macroscopic mechanical behavior of trabecular bone by fabric-based tensors reflecting the morphology. With the exception of Natali et al. (2008b), all other models made use of two internal variables to describe the nonlinearity occurring beyond the yield point. These variables were linked to the loss of stiffness and to the accumulation of residual strain, experimentally observed for both compact and trabecular bone (Fondrk et al. 1999b; Keaveny et al. 2001) and in mechanical

terms described as damage and plasticity. None of the models mentioned so far considered the softening of trabecular bone, manifested by decreasing stress under increasing strain.

In compression, the mechanical behavior of compact and trabecular bone presents distinct characteristics. Compact bone is quasi-brittle, while the mechanical behavior of trabecular bone is typical of an elastoplastic cellular material (Gibson and Ashby 1999; Hayes and Carter 1976). For both types of bone under compressive monotonic loading, the tangent stiffness decreases already before the maximum force is reached. For trabecular bone, a smooth and gradual reduction of the stress (softening) then occurs until a local minimum, followed by slight rehardening (Gibson and Ashby 1999).

The proposed model aims at describing the mechanical behavior of trabecular bone in the range of small to moderate compressive strains and thus considers simultaneous accumulation of plastic deformation and damage that eventually leads to softening. Softening is one of the destabilizing factors that may lead to localization of inelastic processes into narrow bands. To avoid pathological sensitivity of the numerical results to the finite element mesh, the model is regularized by a nonlocal formulation based on a spatial averaging procedure, which acts as a localization limiter (Bažant and Jirásek 2002).

Section 2 of the paper describes the theoretical formulation developed within the framework of plasticity coupled with damage. The description of model parameters is provided in Sect. 3, and numerical aspects are discussed in detail in Sect. 4. Section 5 introduces the nonlocal technique that limits the localization, and finally in Sect. 6 some numerical examples are presented to illustrate the behavior of the model and the impact of softening on the results of complex bone structure simulations.

The intrinsic notation will be used, with vectors represented by lower case bold letters, e.g. $\mathbf{a}$, second-order tensors by upper case bold letters, e.g. $\mathbf{A}$, and fourth-order tensors by fonts with relief, e.g. $\mathbb{A}$. The tensor products $\mathbf{a}\otimes\mathbf{b}$, $\mathbf{A}\otimes\mathbf{B}$ and $\mathbf{A}\,\overline{\otimes}\,\mathbf{B}$ correspond respectively to $a_i b_j$, $A_{ij} B_{kl}$ and $\frac{1}{2}(A_{ik}B_{jl} + A_{il}B_{jk})$ in index notation. Finally, a dot indicates contraction and a colon indicates double contraction.

2 Constitutive model: general framework

This section presents the local constitutive model which is specific to trabecular bone in compression. A general description and framework for elastoplasticity coupled with damage can be found e.g. in Hansen and Schreyer (1994), Lubarda and Krajcinovic (1995), Maugin (1992), Zysset and Curnier (1996).

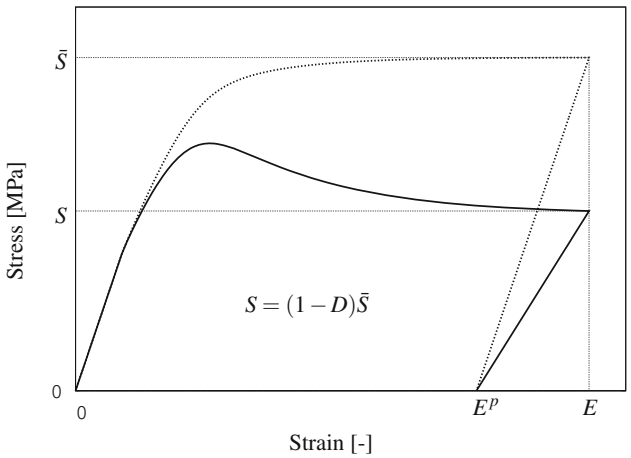

Fig. 1 Stress-strain diagram of the plastic part of the model plotted in terms of the effective stress (*dotted line*) and of the complete model (with damage) plotted in terms of the nominal stress (*continuous line*)

2.1 Rheological model

To motivate the development, we start from a rheological model that possesses the desired characteristics, namely, simultaneous accumulation of plasticity and damage. The plastic part of the model exhibits hardening with saturation, i.e., the yield stress grows and asymptotically approaches a finite limit (Fig. 1). Softening is attributed to the development of damage (Fig. 1). The model is rate independent.

The formulation is based on three state variables. The total strain $\mathbf{E} \in \mathbf{Sym}$ (Green-Lagrange strain tensor) is the observable variable. **Sym** is the set of symmetric second-order tensors. To account for plasticity and damage, we use two internal variables: the plastic strains $\mathbf{E}^p \in \mathbf{Sym}$ and a scalar κ that drives the hardening process and the evolution of the scalar damage parameter $D \in [0, D_C]$, where $D_C \in (0, 1)$ is a critical damage value and κ is the cumulated plastic strain, as will be seen later. The damage parameter D represents the ratio between the number of broken elastoplastic units and the total number of units.

The rheological model in Fig. 2 is composed of identical elastoplastic units placed in parallel, each of them consisting of an elastic spring and a plastic pad arranged in series. Green-Naghdi decomposition of the finite strain tensor is used, $\mathbf{E} = \mathbf{E}^{\mathbf{e}} + \mathbf{E}^p$, where $\mathbf{E}^{\mathbf{e}}$ is the elastic strain (Green and Naghdi 1965). The yield function evolves with κ to reflect isotropic plastic hardening. Softening is incorporated through the damage part of the model.

The model parameters include a fourth-order positive definite elasticity tensor $\mathbb{S}$ characterizing the elastic spring in the elastoplastic unit, and a fourth-order positive semi-definite tensor $\mathbb{F}$ used in the plastic yield function. A complete description is provided in Sect. 3.

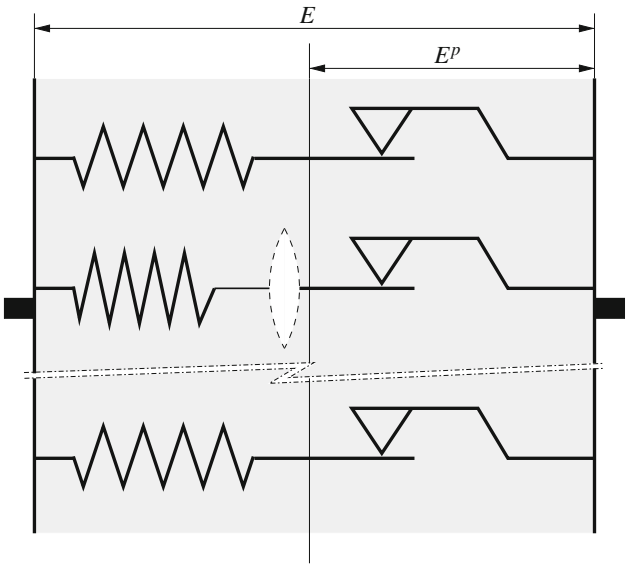

Fig. 2 Rheological model composed of gradually breaking elastoplastic units, each of which exhibits isotropic hardening

2.2 Basic equations

The constitutive model works with two kinds of stress. The effective stress, $\bar{\mathbf{S}}$, is the stress transmitted by the yet unbroken elastoplastic units and is considered as force per unit undamaged area. It is linked to the elastic strain $\mathbf{E^e} = \mathbf{E} - \mathbf{E}^p$ by the generalized Hooke's law

$$\bar{\mathbf{S}} = \mathbb{S}(\mathbf{E} - \mathbf{E}^p) \tag{1}$$

where $\mathbb{S}$ is the elastic stiffness tensor. From a physical perspective, the effective stress can be interpreted as the average stress acting on the effective area of the material, assuming that damage is a relative measure of decohesion in the material (Kachanov 1986; Lemaitre and Chaboche 1994).

The total stress, $\mathbf{S}$, is considered as force per unit total area, and is obtained from the effective stress by taking into account the effect of damage.[1] The present model uses a simple reduction by a scalar factor $1 - D$, where D is the damage variable that describes the reduction of stiffness due to propagation of voids and cracks, and due to breakage of individual trabeculae. The total stress is therefore evaluated as

$$\mathbf{S} = (1 - D(\kappa))\bar{\mathbf{S}} = (1 - D(\kappa))\mathbb{S}(\mathbf{E} - \mathbf{E}^p) \tag{2}$$

where κ is an internal variable that drives the evolution of damage. In the present model, κ is taken as the cumulated plastic strain, so that the damage process is coupled to plastic yielding. The damage variable D evolves monotonically from its initial value 0 to its ultimate value D_c as κ grows from zero to infinity. This is described by the damage function $D(\kappa)$.

To complete the formulation, the evolution of the inelastic variables $\mathbf{E}^p$ and κ must be defined. The plastic part of the model is chosen to be associative and, as mentioned earlier, to be governed by the effective stress. Therefore, the yield function

$$f(\bar{\mathbf{S}}, \kappa) = \sqrt{\bar{\mathbf{S}}:\mathbb{F}\bar{\mathbf{S}}} - \bar{\sigma}^p(\kappa) \tag{3}$$

is defined as the difference between a generalized seminorm of the effective stress and the current yield stress $\bar{\sigma}^p$, which directly depends on the cumulated plastic strain κ. Evolution of plastic strain is described by the normality rule

$$\dot{\mathbf{E}}^p = \dot{\lambda}\frac{\partial f(\bar{\mathbf{S}}, \kappa)}{\partial \bar{\mathbf{S}}} \tag{4}$$

combined with the usual loading–unloading conditions

$$f(\bar{\mathbf{S}}, \kappa) \le 0, \quad \dot{\lambda} \ge 0, \quad \dot{\lambda} f(\bar{\mathbf{S}}, \kappa) = 0 \tag{5}$$

in which $\dot{\lambda}$ is the rate of the plastic multiplier. These conditions imply that

1. if $f(\bar{\mathbf{S}}, \kappa) < 0$ we have $\dot{\lambda} = 0$ and the material response is elastic (no plastic flow),
2. if $f(\bar{\mathbf{S}}, \kappa) = 0$ we can have $\dot{\lambda} > 0$ and plastic flow may occur, and
3. $f(\bar{\mathbf{S}}, \kappa) > 0$ is not admissible.

According to (4), the yield function f plays the role of the plastic potential. Substituting the specific form of the yield function (3) into (4), we obtain

$$\dot{\mathbf{E}}^p = \dot{\lambda}\frac{\mathbb{F}\bar{\mathbf{S}}}{\sqrt{\bar{\mathbf{S}}:\mathbb{F}\bar{\mathbf{S}}}} \tag{6}$$

The cumulated plastic strain κ is defined by the evolution equation

$$\dot{\kappa} = \|\dot{\mathbf{E}}^p\| = \sqrt{\dot{\mathbf{E}}^p:\dot{\mathbf{E}}^p} \tag{7}$$

from which

$$\kappa(t) = \int_0^t \dot{\kappa}(\tau)\,\mathrm{d}\tau = \int_0^t \sqrt{\dot{\mathbf{E}}^p(\tau):\dot{\mathbf{E}}^p(\tau)}\,\mathrm{d}\tau \tag{8}$$

Substituting the flow rule (6) into Eq. (7), we obtain the relation between the rate of the plastic multiplier and the rate of the cumulated plastic strain:

$$\dot{\kappa} = \left\| \dot{\lambda}\frac{\mathbb{F}\bar{\mathbf{S}}}{\sqrt{\bar{\mathbf{S}}:\mathbb{F}\bar{\mathbf{S}}}} \right\| = \dot{\lambda}\frac{\|\mathbb{F}\bar{\mathbf{S}}\|}{\sqrt{\bar{\mathbf{S}}:\mathbb{F}\bar{\mathbf{S}}}} \tag{9}$$

[1] In damage mechanics, this kind of stress is sometimes called nominal (as opposed to effective), but this may lead to confusion with the first Piola–Kirchhoff stress. The stress used here corresponds to the second Piola–Kirchhoff stress and therefore we prefer to avoid the adjective "nominal" and replace it by "total".

Therefore, $\dot{\lambda}$ can be expressed in terms of $\dot{\kappa}$ and the flow rule can be rewritten as

$$\dot{\mathbf{E}}^p = \dot{\kappa}\frac{\mathbb{F}\bar{\mathbf{S}}}{\|\mathbb{F}\bar{\mathbf{S}}\|} = \dot{\kappa}\mathbf{N}^p \tag{10}$$

where

$$\mathbf{N}^p = \frac{\mathbb{F}\bar{\mathbf{S}}}{\|\mathbb{F}\bar{\mathbf{S}}\|} \tag{11}$$

is a normalized tensor indicating the plastic flow direction, while $\dot{\kappa}$ indicates the magnitude of plastic flow.

As shown in Grassl and Jirásek (2006a), if the yield function is formulated in terms of effective stress, local uniqueness of the solution (any prescribed strain history generates a unique response) requires less restrictive conditions than if the total stress is used. In the current formulation, with associated plasticity and monotonic positive plastic hardening, local uniqueness is always ensured.

2.3 Thermodynamic aspects

For the model to be thermodynamically admissible, the rate of dissipation must always remain nonnegative, which is a consequence of the second law of thermodynamics. At constant temperature, the dissipation rate

$$\mathscr{D} = \mathbf{S}{:}\dot{\mathbf{E}} - \dot{\psi} \tag{12}$$

can be computed as the difference between the stress power density and the rate of Helmholtz free energy density. A plausible choice of the expression for the free energy density of an elastoplastic material with damage is

$$\psi(\mathbf{E}, \mathbf{E}^p, \kappa) = \tfrac{1}{2}\,(1 - D(\kappa))\,(\mathbf{E} - \mathbf{E}^p){:}\mathbb{S}(\mathbf{E} - \mathbf{E}^p) \tag{13}$$

The dissipation rate then becomes

$$\begin{aligned}\mathscr{D} = {}& \mathbf{S}{:}\dot{\mathbf{E}} - (1 - D(\kappa))\,\mathbb{S}(\mathbf{E} - \mathbf{E}^p){:}\dot{\mathbf{E}} \\ & + (1 - D(\kappa))\,\mathbb{S}(\mathbf{E} - \mathbf{E}^p){:}\dot{\mathbf{E}}^p \\ & + \tfrac{1}{2}(\mathbf{E} - \mathbf{E}^p){:}\mathbb{S}(\mathbf{E} - \mathbf{E}^p)\,D_{,\kappa}\dot{\kappa}\end{aligned} \tag{14}$$

where $D_{,\kappa} = \mathrm{d}D(\kappa)/\mathrm{d}\kappa$ is the derivative of the damage function with respect to the cumulated plastic stress. By virtue of (2), the first two terms on the right-hand side cancel and the dissipation inequality can be written as

$$\mathscr{D} = \mathscr{D}_p + \mathscr{D}_D \geq 0 \tag{15}$$

where

$$\mathscr{D}_p = (1 - D(\kappa))\,\mathbb{S}(\mathbf{E} - \mathbf{E}^p){:}\dot{\mathbf{E}}^p = \mathbf{S}{:}\dot{\mathbf{E}}^p \tag{16}$$

is the plastic dissipation rate and

$$\mathscr{D}_D = \tfrac{1}{2}(\mathbf{E} - \mathbf{E}^p){:}\mathbb{S}(\mathbf{E} - \mathbf{E}^p)\,D_{,\kappa}\dot{\kappa} \tag{17}$$

is the damage dissipation rate.

For condition (15) to be verified, it is sufficient to show that $\mathscr{D}_p \geq 0$ and $\mathscr{D}_D \geq 0$. Since the elastic stiffness tensor $\mathbb{S}$ is positive definite and $\dot{\kappa} = \|\dot{\mathbf{E}}^p\|$ is always nonnegative, the damage dissipation inequality (17) is verified if $D_{,\kappa}$ is nonnegative, which means that damage cannot decrease. This is a very natural requirement, as long as we do not consider bone healing, which would require a much broader framework.

Using Eqs. (10) and (2), the plastic dissipation (16) can be rewritten in the form

$$\mathscr{D}_p = \dot{\kappa}\;\mathbf{S}{:}\frac{\mathbb{F}\bar{\mathbf{S}}}{\|\mathbb{F}\bar{\mathbf{S}}\|} = \frac{\dot{\kappa}\,(1 - D(\kappa))}{\|\mathbb{F}\bar{\mathbf{S}}\|}\bar{\mathbf{S}}{:}\mathbb{F}\bar{\mathbf{S}} \tag{18}$$

Since $D(\kappa) \leq 1$ and $\dot{\kappa} \geq 0$, the fraction on the right-hand side of (18) is always nonnegative, and since $\mathbb{F}$ is positive semi-definite, the product $\bar{\mathbf{S}}{:}\mathbb{F}\bar{\mathbf{S}}$ is also nonnegative. Therefore, the plastic dissipation is always nonnegative and the dissipation inequality is verified.

3 Constitutive model: specific details

3.1 Morphology and fabric tensor

The purpose of the model is to describe the constitutive behavior of trabecular bone using a continuum description at the macroscopic scale (e.g. Crawford et al. 2003; Chevalier et al. 2008a). In this approach, the trabecular bone structure is homogenized using morphological parameters obtained from computed tomography. The porosity of the trabecular bone is described by the bone volume fraction $\rho \in]0, 1]$, while its anisotropy (actually limited to orthotropy) is reflected by a second-order symmetric positive definite tensor $\mathbf{M}$, presented in terms of its spectral decomposition

$$\mathbf{M} = \sum_{i=1}^{3} m_i\,(\mathbf{m}_i \otimes \mathbf{m}_i) \tag{19}$$

Here, $m_i, i = 1, 2, 3$, are the eigenvalues, and $\mathbf{m}_i, i = 1, 2, 3$, are the corresponding unit eigenvectors, which specify the orientation of the axes of orthotropy. The eigenvalues are normalized such that $\mathrm{Tr}\,(\mathbf{M}) = 3$. For an isotropic material, all eigenvalues are equal to 1 and $\mathbf{M}$ becomes a unit tensor.

Similar to Garcia et al. (2009), the constitutive model makes use of fourth-order tensors based on morphology and related to the fabric tensor, as described in Curnier et al. (1995), Zysset and Curnier (1995), Zysset (2003), Zysset and Rincón (2006). For completeness, the basic ideas will be briefly recalled in the next two subsections. After that, we will specify the hardening function and the damage law, both dependent on the cumulated plastic strain.

3.2 Elastic stiffness and compliance

The fourth-order elastic compliance tensor $\mathbb{E}$ corresponds to an orthotropic material with principal directions given by the

eigenvectors $\mathbf{m}_i$ of the fabric tensor. The compliance coefficients are scaled with the bone volume fraction ρ and with the eigenvalues m_i of the fabric tensor. In Voigt notation, the elastic compliance is represented by the matrix

$$\mathbb{E} = \begin{bmatrix} \frac{1}{\varepsilon_1} & -\frac{\nu_{12}}{\varepsilon_1} & -\frac{\nu_{13}}{\varepsilon_1} & 0 & 0 & 0 \\ -\frac{\nu_{21}}{\varepsilon_2} & \frac{1}{\varepsilon_2} & -\frac{\nu_{23}}{\varepsilon_2} & 0 & 0 & 0 \\ -\frac{\nu_{31}}{\varepsilon_3} & -\frac{\nu_{32}}{\varepsilon_3} & \frac{1}{\varepsilon_3} & 0 & 0 & 0 \\ 0 & 0 & 0 & \frac{1}{\mu_{23}} & 0 & 0 \\ 0 & 0 & 0 & 0 & \frac{1}{\mu_{31}} & 0 \\ 0 & 0 & 0 & 0 & 0 & \frac{1}{\mu_{12}} \end{bmatrix} \tag{20}$$

with the elastic moduli given by

$$\varepsilon_i = \varepsilon_0 \rho^k m_i^{2l} \tag{21}$$

$$\mu_{ij} = \mu_0 \rho^k m_i^l m_j^l \tag{22}$$

and the Poisson ratios by

$$\nu_{ij} = \nu_0 \frac{m_i^l}{m_j^l} \tag{23}$$

Constants ε_0, μ_0 and ν_0 are the elastic properties of a fictitious bone material with zero porosity, and dimensionless exponents k and l are determined by fitting of experimental results.

The elastic stiffness tensor $\mathbb{S} = \mathbb{E}^{-1}$ is the inverse of the elastic compliance tensor, and its explicit representation is given in Zysset (2003). When this linear elasticity model is formulated with large strain and stress measures, it holds exactly only at the origin and is then progressively influenced by the geometrical nonlinearity.

3.3 Yield criterion

Similar to Garcia et al. (2009), the tensile-compressive asymmetry of the yield stress is described using a piecewise quadratic generalized Hill criterion (Zysset and Rincón 2006). The compressive and tensile parts of the yield surface meet at the hyperplane given by

$$\hat{\mathbf{N}} : \bar{\mathbf{S}} = 0 \tag{24}$$

where $\hat{\mathbf{N}}$ is a tensor orthogonal to that hyperplane (to be specified later, see (29)). Consequently, the tensor $\mathbb{F}$ that appears in the yield function (3) is different in each part of the effective stress space. This tensor will be denoted as $\mathbb{F}^+$ in the tensile part, characterized by $\hat{\mathbf{N}} : \bar{\mathbf{S}} \geq 0$, and as $\mathbb{F}^-$ in the compressive part, characterized by $\hat{\mathbf{N}} : \bar{\mathbf{S}} \leq 0$. Of course, $\mathbb{F}^+$ and $\mathbb{F}^-$ are not completely independent, because continuity of the yield surface must be preserved. Therefore, for all effective stress states $\bar{\mathbf{S}}$ satisfying the condition $\hat{\mathbf{N}} : \bar{\mathbf{S}} = 0$ we must have $\bar{\mathbf{S}}{:}\mathbb{F}^+\bar{\mathbf{S}} = \bar{\mathbf{S}}{:}\mathbb{F}^-\bar{\mathbf{S}}$.

The general structure of the fourth-order tensors $\mathbb{F}^+$ and $\mathbb{F}^-$ is the same as for the elastic compliance tensor. In the Voigt notation, these tensors are represented by the matrices

$$\mathbb{F}^\pm = \begin{bmatrix} \frac{1}{(\sigma_1^\pm)^2} & -\frac{\chi_{12}^\pm}{(\sigma_1^\pm)^2} & -\frac{\chi_{13}^\pm}{(\sigma_1^\pm)^2} & 0 & 0 & 0 \\ -\frac{\chi_{21}^\pm}{(\sigma_2^\pm)^2} & \frac{1}{(\sigma_2^\pm)^2} & -\frac{\chi_{23}^\pm}{(\sigma_2^\pm)^2} & 0 & 0 & 0 \\ -\frac{\chi_{31}^\pm}{(\sigma_3^\pm)^2} & -\frac{\chi_{32}^\pm}{(\sigma_3^\pm)^2} & \frac{1}{(\sigma_3^\pm)^2} & 0 & 0 & 0 \\ 0 & 0 & 0 & \frac{1}{\tau_{23}^2} & 0 & 0 \\ 0 & 0 & 0 & 0 & \frac{1}{\tau_{31}^2} & 0 \\ 0 & 0 & 0 & 0 & 0 & \frac{1}{\tau_{12}^2} \end{bmatrix} \tag{25}$$

where

$$\sigma_i^\pm = \sigma_0^\pm \rho^p m_i^{2q} \tag{26}$$

are the initial uniaxial tensile and compressive yield stresses along individual axes of orthotropy,

$$\tau_{ij} = \tau_0 \rho^p m_i^q m_j^q \tag{27}$$

are the initial yield stresses in shear in the planes of orthotropy, and

$$\chi_{ij}^\pm = \chi_0^\pm \frac{m_i^{2q}}{m_j^{2q}} \tag{28}$$

are the interaction coefficients. Exponents p and q in (26)–(28), which reflect the influence of the bone volume fraction and fabric, are in general different from exponents k and l used in expressions (21)–(23) for the elastic constants. Parameters $\sigma_0^\pm$, τ_0 and $\chi_0^\pm$ correspond to the properties of a fictitious material with zero porosity. As shown by Zysset and Rincón (2006), the condition of continuous differentiability of the yield surface (across the hyperplane separating its tensile and compressive parts) is satisfied if the tensor normal to the hyperplane is defined as

$$\hat{\mathbf{N}} = \frac{\sum_{i=1}^3 m_i^{-2q}}{\sqrt{\sum_{i=1}^3 m_i^{-4q}}} (\mathbf{m}_i \otimes \mathbf{m}_i) \tag{29}$$

and if the parameter values are constrained by the condition

$$\frac{\chi_0^- + 1}{(\sigma_0^-)^2} = \frac{\chi_0^+ + 1}{(\sigma_0^+)^2} \tag{30}$$

3.4 Plastic hardening

The plastic hardening function describes the growth of the yield stress beyond the initial yield point. We consider an exponential hardening function, which asymptotically approaches a limit value. Note that softening of the total stress can be taken into account by the damage part of the model,

and so, in terms of total stress, a purely hardening behavior with saturation is sufficient. Using hardening plasticity with associated flow has a positive effect on the robustness of the numerical algorithm, because the stress return is equivalent to a convex minimization problem, which always has a unique solution.

Since the physical dimension of tensor $\mathbb{F}$ is chosen such that the product $\bar{\mathbf{S}}{:}\mathbb{F}\bar{\mathbf{S}}$ is dimensionless, the yield value $\bar{\sigma}^p$ must be dimensionless as well, and it corresponds to the ratio between the current yield stress and the initial one. The exponential hardening function is then

$$\bar{\sigma}^p = 1 + \sigma^H(1 - \mathrm{e}^{-s\kappa}) \tag{31}$$

where σ^H and s are two nonnegative dimensionless parameters, to be identified from experiments.

3.5 Damage evolution

The growth of damage, driven by the cumulated plastic strain, is also described using an exponential function

$$D(\kappa) = D_C(1 - \mathrm{e}^{-a\kappa}) \tag{32}$$

with the derivative with respect to κ given by

$$D_{,\kappa}(\kappa) = \frac{\mathrm{d}D(\kappa)}{\mathrm{d}\kappa} = D_C a \mathrm{e}^{-a\kappa} \tag{33}$$

Dimensionless parameters $a \geq 0$ and $D_C < 1$ control the softening part of the stress-strain diagram.

4 Numerical algorithm

To implement the constitutive model into a finite element code, the basic equations need to be rewritten in an incremental form, and a stress evaluation algorithm needs to be developed (Simo and Taylor 1985; Zysset 1994; Rakotomanana et al. 1991; Simo and Hughes 2000; Grassl and Jirásek 2006a). At the global (structural) level, the nonlinear equilibrium equations are solved using a Newton–Raphson scheme, which requires an algorithmic (consistent) stiffness obtained by differentiation of the incremental stress evaluation procedure.

The following subsection presents the solution of the incremental strain-driven problem. Afterward, the continuum and algorithmic tangent operators are presented.

4.1 Stress evaluation algorithm

For the present purpose, we introduce subscripts n and $n+1$ that respectively correspond to the values at the beginning of the step (converged values of the preceding step) and at the end of the step. The plastic part of the model has been formulated in the effective stress space, and so the plastic stress return algorithm provides the effective stress. The damage part of the model then gives the total stress.

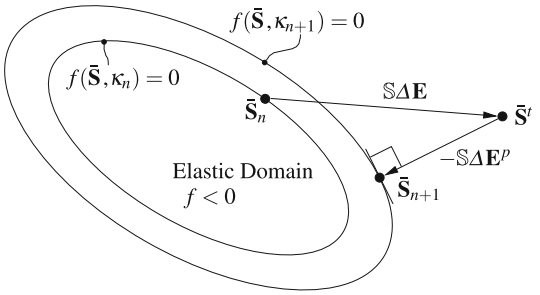

Fig. 3 Graphical representation of the plastic stress return algorithm for a model with isotropic hardening and associated plastic flow in the effective stress space

In the context of the displacement-based finite element method, the strain $\mathbf{E}_{n+1} = \mathbf{E}_n + \Delta\mathbf{E}$ at the end of the increment is estimated by solving the linearized equilibrium equations, and is considered as input into the stress evaluation algorithm. All other variables, such as the effective and nominal stress, plastic strain, cumulative plastic strain or damage, are known only at the beginning of the step, and the purpose of the stress evaluation algorithm is to determine their values at the end of the step, such that all the governing equations are satisfied. The effective stress can be directly computed from the total and plastic strain, the damage variable uniquely depends on the cumulative plastic strain, and the nominal stress can be obtained from the effective stress and damage. It is therefore sufficient to specify $\mathbf{E}_{n+1}$, $\mathbf{E}^p_n$ and κ_n as the input variables.

4.1.1 Plastic stress return

The plastic strain increment is first set to zero, and the corresponding trial stress

$$\bar{\mathbf{S}}^t = \mathbb{S}(\mathbf{E}_{n+1} - \mathbf{E}^p_n) \tag{34}$$

is computed. It corresponds to a tentative solution for which plastic admissibility must be tested.

If $f(\bar{\mathbf{S}}^t, \kappa_n) \leq 0$, the increment is indeed elastic and there is no evolution of the plastic strain and damage. The solution of the incremental problem is then simply $\bar{\mathbf{S}}_{n+1} = \bar{\mathbf{S}}^t$, $\mathbf{E}^p_{n+1} = \mathbf{E}^p_n$, $\kappa_{n+1} = \kappa_n$ and $D_{n+1} = D_n = D(\kappa_n)$.

On the other hand, if $f(\bar{\mathbf{S}}^t, \kappa_n) > 0$, plastic flow occurs during the increment and the solution is found using a stress-return algorithm (Fig. 3). The current development is similar to Zysset (1994). The primary unknown variables $\bar{\mathbf{S}}_{n+1}$ and $\Delta\kappa$ need to be solved from a system of nonlinear equations.

The first equation to be satisfied is the yield condition at the end of the step:

$$\sqrt{\bar{\mathbf{S}}_{n+1}{:}\mathbb{F}\bar{\mathbf{S}}_{n+1}} - \bar{\sigma}^p(\kappa_n + \Delta\kappa) = 0 \tag{35}$$

Since $\mathbf{E}^p_{n+1} = \mathbf{E}^p_n + \Delta\mathbf{E}^p$, the effective stress at the end of the step can be expressed as

$$\bar{\mathbf{S}}_{n+1} = \mathbb{S}(\mathbf{E}_{n+1} - \mathbf{E}^p_n - \Delta\mathbf{E}^p) = \bar{\mathbf{S}}^t - \mathbb{S}\,\Delta\mathbf{E}^p \tag{36}$$

Based on the flow rule (10), the plastic strain increment is approximated using the backward Euler formula

$$\Delta\mathbf{E}^p = \Delta\kappa\,\mathbf{N}^p_{n+1} \tag{37}$$

where

$$\mathbf{N}^p_{n+1} = \frac{\mathbb{F}\bar{\mathbf{S}}_{n+1}}{\|\mathbb{F}\bar{\mathbf{S}}_{n+1}\|} \tag{38}$$

is the direction of plastic flow at the end of the step. Substituting (37)–(38) into (36), we obtain

$$\bar{\mathbf{S}}_{n+1} = \bar{\mathbf{S}}^t - \Delta\kappa\frac{\mathbb{S}\mathbb{F}\bar{\mathbf{S}}_{n+1}}{\|\mathbb{F}\bar{\mathbf{S}}_{n+1}\|} \tag{39}$$

Equations (39) and (35) represent a set of nonlinear equations for unknowns $\bar{\mathbf{S}}_{n+1}$ and $\Delta\kappa$. For convenience, they are rewritten as

$$\mathbf{R}(\bar{\mathbf{S}}_{n+1}, \Delta\kappa) \equiv \mathbb{E}(\bar{\mathbf{S}}_{n+1} - \bar{\mathbf{S}}^t) + \Delta\kappa\mathbf{N}^p_{n+1} = 0 \tag{40}$$

$$f(\bar{\mathbf{S}}_{n+1}, \Delta\kappa) \equiv \sqrt{\bar{\mathbf{S}}_{n+1}:\mathbb{F}\bar{\mathbf{S}}_{n+1}} - \bar{\sigma}^p(\kappa_n + \Delta\kappa) = 0 \tag{41}$$

These equations can be solved iteratively by the Newton–Raphson method. Their linearized form is

$$\mathbf{R}^{i+1} \approx \mathbf{R}^i + \frac{\partial\mathbf{R}^i}{\partial\bar{\mathbf{S}}_{n+1}}\delta\bar{\mathbf{S}}_{n+1} + \frac{\partial\mathbf{R}^i}{\partial\Delta\kappa}\delta\Delta\kappa = 0 \tag{42}$$

$$f^{i+1} \approx f^i + \frac{\partial f^i}{\partial\bar{\mathbf{S}}_{n+1}}:\delta\bar{\mathbf{S}}_{n+1} + \frac{\partial f^i}{\partial\Delta\kappa}\delta\Delta\kappa = 0 \tag{43}$$

where $\delta\bar{\mathbf{S}}_{n+1}$ and $\delta\Delta\kappa$ are the iterative corrections of $\bar{\mathbf{S}}^i_{n+1}$ and $\Delta\kappa^i$. Superscript i indicates the iteration number, not to confuse with subscript n, which is the step number. Note that we have simplified the writing by shorthand notation such as $\mathbf{R}^i = \mathbf{R}(\mathbf{S}^i_{n+1}, \Delta\kappa^i)$. For each iteration i, the solution of (42)–(43) is obtained as

$$\delta\Delta\kappa = \frac{\frac{\sqrt{\bar{\mathbf{S}}^i_{n+1}:\mathbb{F}\bar{\mathbf{S}}^i_{n+1}}}{\|\mathbb{F}\bar{\mathbf{S}}^i_{n+1}\|}f^i - \mathbf{N}^{p,i}_{n+1}:\mathbb{S}^i_{a,n+1}\mathbf{R}^i}{\mathbf{N}^{p,i}_{n+1}:\mathbb{S}^i_{a,n+1}\mathbf{N}^{p,i}_{n+1} + \frac{\sqrt{\bar{\mathbf{S}}^i_{n+1}:\mathbb{F}\bar{\mathbf{S}}^i_{n+1}}}{\|\mathbb{F}\bar{\mathbf{S}}^i_{n+1}\|}\bar{\sigma}^{p,i}_{,\kappa}} \tag{44}$$

$$\delta\bar{\mathbf{S}}_{n+1} = -\mathbb{S}^i_{a,n+1}\left(\mathbf{R}^i + \mathbf{N}^{p,i}_{n+1}\delta\Delta\kappa\right) \tag{45}$$

where $\bar{\sigma}^{p,i}_{,\kappa} = \sigma^H s\,\mathrm{e}^{-s(\kappa_n+\Delta\kappa^i)}$, $\mathbf{N}^{p,i}_{n+1} = \frac{\mathbb{F}\bar{\mathbf{S}}^i_{n+1}}{\|\mathbb{F}\bar{\mathbf{S}}^i_{n+1}\|}$, and

$$\mathbb{S}^i_{a,n+1} = \left[\mathbb{E} + \frac{\Delta\kappa^i}{\|\mathbb{F}\bar{\mathbf{S}}^i_{n+1}\|}\left(\mathbb{F} - \mathbf{N}^{p,i}_{n+1}\otimes\mathbb{F}\mathbf{N}^{p,i}_{n+1}\right)\right]^{-1} \tag{46}$$

The improved approximation of the solution of (40)–(41) is $\bar{\mathbf{S}}^{i+1}_{n+1} = \bar{\mathbf{S}}^i_{n+1} + \delta\bar{\mathbf{S}}_{n+1}$ and $\Delta\kappa^{i+1} = \Delta\kappa^i + \delta\Delta\kappa$.

The iterative process is repeated until the norm of $\mathbf{R}^{i+1}$ and the magnitude of f^{i+1} are below a prescribed tolerance. At this stage, we obtain the converged effective stress $\bar{\mathbf{S}}_{n+1} = \bar{\mathbf{S}}^{i+1}_{n+1}$ and the increment of cumulated plastic strain $\Delta\kappa = \Delta\kappa^{i+1}$, and we can update

$$\mathbf{E}^p_{n+1} = \mathbf{E}^p_n + \Delta\kappa\frac{\mathbb{F}\bar{\mathbf{S}}_{n+1}}{\|\mathbb{F}\bar{\mathbf{S}}_{n+1}\|} \tag{47}$$

$$\kappa_{n+1} = \kappa_n + \Delta\kappa \tag{48}$$

The updated cumulated plastic strain κ_{n+1} is then used to compute the damage.

4.1.2 Damage evaluation

The damage variable at the end of the step is easily obtained by substituting the updated cumulated plastic strain κ_{n+1} into the damage law (32):

$$D_{n+1} = D(\kappa_{n+1}) = D_C(1 - e^{-a\kappa_{n+1}}) \tag{49}$$

After that, the total stress is evaluated as

$$\mathbf{S}_{n+1} = (1 - D_{n+1})\bar{\mathbf{S}}_{n+1} \tag{50}$$

4.2 Tangent stiffness tensors

Implementation of the model into a finite element code using the Newton–Raphson iterative scheme requires the evaluation of the algorithmic tangent stiffness, which provides a quadratic convergence rate. The algorithmic tangent operator comes from the linearization of the stress evaluation algorithm that deals with a finite increment. In general, it is different from the continuum tangent operator, which links the strain rate to the corresponding stress rate.

4.2.1 Continuum stiffness

Taking the time derivative of stress-strain laws (1) and (2), we obtain

$$\dot{\bar{\mathbf{S}}} = \mathbb{S}(\dot{\mathbf{E}} - \dot{\mathbf{E}}^p) \tag{51}$$

$$\dot{\mathbf{S}} = (1 - D)\dot{\bar{\mathbf{S}}} - \dot{D}\bar{\mathbf{S}} = (1 - D)\mathbb{S}(\dot{\mathbf{E}} - \dot{\mathbf{E}}^p) - D_{,\kappa}\bar{\mathbf{S}}\dot{\kappa} \tag{52}$$

The plastic strain rate can be eliminated using the flow rule (10), which gives

$$\dot{\bar{\mathbf{S}}} = \mathbb{S}\dot{\mathbf{E}} - \mathbb{S}\mathbf{N}^p\dot{\kappa} \tag{53}$$

$$\dot{\mathbf{S}} = (1 - D)\mathbb{S}\dot{\mathbf{E}} - \left((1 - D)\mathbb{S}\mathbf{N}^p + D_{,\kappa}\bar{\mathbf{S}}\right)\dot{\kappa} \tag{54}$$

When no plastic flow occurs, we have $\dot{\kappa} = 0$, and the relation between the rates of strain and total stress is described by the secant (damaged) stiffness tensor

$$\mathbb{S}^D = (1 - D)\mathbb{S} \tag{55}$$

During plastic flow, the yield function remains equal to zero, and its time derivative vanishes. Differentiation of the yield function (3) leads to

$$\dot{f} = \frac{\bar{\mathbf{S}} : \mathbb{F}\dot{\bar{\mathbf{S}}}}{\sqrt{\bar{\mathbf{S}} : \mathbb{F}\bar{\mathbf{S}}}} - \bar{\sigma}^p_{,\kappa}\dot{\kappa} \tag{56}$$

The expression in the denominator can be replaced by $\bar{\sigma}^p$, because during plastic flow the yield function is equal to zero, and the effective stress rate can be replaced by the right-hand side of (53). The consistency condition

$$\dot{f} = \frac{1}{\bar{\sigma}^p}\bar{\mathbf{S}} : \mathbb{F}\mathbb{S}(\dot{\mathbf{E}} - \mathbf{N}^p\dot{\kappa}) - \bar{\sigma}^p_{,\kappa}\dot{\kappa} = 0 \tag{57}$$

then represents a scalar equation from which the rate of cumulated plastic strain can be expressed in terms of the strain rate:

$$\dot{\kappa} = \frac{\bar{\mathbf{S}} : \mathbb{F}\mathbb{S}\dot{\mathbf{E}}}{\bar{\mathbf{S}} : \mathbb{F}\mathbb{S}\mathbf{N}^p + \bar{\sigma}^p\bar{\sigma}^p_{,\kappa}} = \frac{\mathbb{S}\mathbf{N}^p}{\mathbf{N}^p : \mathbb{S}\mathbf{N}^p + \bar{\sigma}^p\bar{\sigma}^p_{,\kappa}/\|\mathbb{F}\bar{\mathbf{S}}\|} : \dot{\mathbf{E}} \tag{58}$$

Elimination of $\dot{\kappa}$ from (53) leads to the relation between the rates of strain and effective stress described by the elastoplastic stiffness tensor

$$\mathbb{S}^P = \mathbb{S} - \frac{\mathbb{S}\mathbf{N}^p \otimes \mathbb{S}\mathbf{N}^p}{\mathbf{N}^p : \mathbb{S}\mathbf{N}^p + \bar{\sigma}^p\bar{\sigma}^p_{,\kappa}/\|\mathbb{F}\bar{\mathbf{S}}\|} \tag{59}$$

Similar to that, elimination of $\dot{\kappa}$ from (54) leads to the relation between the rates of strain and total stress described by the damaged elastoplastic stiffness tensor

$$\mathbb{S}^{DP} = (1-D)\mathbb{S} - \frac{\big((1-D)\mathbb{S}\mathbf{N}^p + D_{,\kappa}\bar{\mathbf{S}}\big) \otimes \mathbb{S}\mathbf{N}^p}{\mathbf{N}^p : \mathbb{S}\mathbf{N}^p + \bar{\sigma}^p\bar{\sigma}^p_{,\kappa}/\|\mathbb{F}\bar{\mathbf{S}}\|} \tag{60}$$

Note that (59) is a special case of (60) with no damage ($D = 0$, $D_{,\kappa} = 0$). Stiffness tensor (59) exhibits major symmetry, as can be expected from an elastoplastic model with an associated rule. In (60), major symmetry is lost due to the effect of damage.

4.2.2 Algorithmic stiffness

In the numerical simulation, the strain increment $\Delta\mathbf{E}$ is given and the corresponding stress increment $\Delta\mathbf{S}$ is computed using the stress evaluation algorithm. The algorithmic stiffness tensor $\mathbb{S}^{DP}_a$ relates infinitesimal changes of the finite strain increment, $\mathrm{d}(\Delta\mathbf{E})$, to the corresponding infinitesimal changes of the finite stress increment, $\mathrm{d}(\Delta\mathbf{S})$.

We will first determine the algorithmic stiffness $\mathbb{S}^P_a$ that refers to the plastic stress return algorithm. Recall that the effective stress at the end of the increment, $\bar{\mathbf{S}}_{n+1}$, is the solution of nonlinear Eqs. (40)–(41) with the trial stress $\bar{\mathbf{S}}^t$ dependent on the strain increment according to (34). If the strain increment $\Delta\mathbf{E}$ changes by $\mathrm{d}(\Delta\mathbf{E})$, the corresponding trial stress changes by $\mathrm{d}\bar{\mathbf{S}}^t = \mathbb{S}\,\mathrm{d}(\Delta\mathbf{E})$ and the corresponding change of $\bar{\mathbf{S}}_{n+1}$ can be found by linearizing (40)–(41) around the original solution. Since the linearization has already been developed in the description of the stress return algorithm, there is no need to repeat it. We can simply reuse Eqs. (42)–(43). The residual in (40) is $\mathrm{d}\mathbf{R} = -\mathbb{E}\,\mathrm{d}\bar{\mathbf{S}}^t = -\mathrm{d}(\Delta\mathbf{E})$, the residual in (41) is $\mathrm{d}f = 0$, and the solution of linearized Eqs. (42)–(43) is given by (44)–(45), where the state with superscript i has to be interpreted as the converged result of the stress-return algorithm for the original strain increment, and the iterative corrections $\delta\Delta\kappa$ and $\delta\bar{\mathbf{S}}_{n+1}$ represent infinitesimal changes $\mathrm{d}(\Delta\kappa)$ and $\mathrm{d}(\Delta\bar{\mathbf{S}})$ of the finite increments $\Delta\kappa$ and $\Delta\bar{\mathbf{S}}$ that correspond to the infinitesimal change $\mathrm{d}(\Delta\mathbf{E})$ of the finite strain increment $\Delta\mathbf{E}$. Therefore, substituting (44) into (45) gives the relation between $\mathrm{d}(\Delta\mathbf{E})$ and $\mathrm{d}(\Delta\bar{\mathbf{S}})$ in the form $\mathrm{d}(\Delta\bar{\mathbf{S}}) = \mathbb{S}^P_a\,\mathrm{d}(\Delta\mathbf{E})$. Working out the details, we obtain the elastoplastic algorithmic stiffness tensor

$$\mathbb{S}^P_a = \mathbb{S}_a - \frac{\mathbb{S}_a\mathbf{N}^p \otimes \mathbb{S}_a^{\mathrm{T}}\mathbf{N}^p}{\mathbf{N}^p : \mathbb{S}_a\mathbf{N}^p + \bar{\sigma}^p\bar{\sigma}^p_{,\kappa}/\|\mathbb{F}\bar{\mathbf{S}}\|} \tag{61}$$

with $\mathbb{S}_a$ defined in Eq. (46). Note that the algorithmic stiffness (61) has the same structure as the continuum stiffness (59), only with the elastic stiffness $\mathbb{S}$ replaced by $\mathbb{S}_a$ given by (46). The difference between $\mathbb{S}_a$ and $\mathbb{S}$ is due to curvature of the yield surface and would vanish if the yield surface was planar. The difference also depends on the size of the increment, entering through $\Delta\kappa$, and vanishes in the limit for the increment size approaching zero. In this limit, the algorithmic stiffness approaches the continuum stiffness.

The complete algorithmic stiffness, which takes into account the influence of damage and links $\mathrm{d}(\Delta\mathbf{E})$ to $\mathbf{S}_{n+1}$, can be constructed easily by linearizing Eq. (2). The resulting expression

$$\mathbb{S}^{DP}_a = (1-D)\mathbb{S}_a - \frac{\big((1-D)\mathbb{S}_a\mathbf{N}^p + D_{,\kappa}\bar{\mathbf{S}}\big) \otimes \mathbb{S}_a^{\mathrm{T}}\mathbf{N}^p}{\mathbf{N}^p : \mathbb{S}_a\mathbf{N}^p + \bar{\sigma}^p\bar{\sigma}^p_{,\kappa}/\|\mathbb{F}\bar{\mathbf{S}}\|} \tag{62}$$

has the same structure as (60), with $\mathbb{S}$ replaced by $\mathbb{S}_a$, and approaches (60) in the limit for the increment size approaching zero.

5 Nonlocal formulation

The motivation for using a nonlocal formulation comes from the need to avoid pathological mesh dependence in boundary value problems that use material laws with softening; see e.g. Bažant and Jirásek (2002). The source of the undesired sensitivity to the finite element size is best explained using a simple one-dimensional model of a bar (Fig. 4) of initial length L, which is fixed at one end and loaded by an increasing displacement u applied at the other end.

If the bar is discretized by finite elements, the response remains uniform as long as the stress keeps increasing under increasing strain, i.e., as long as the material behavior is

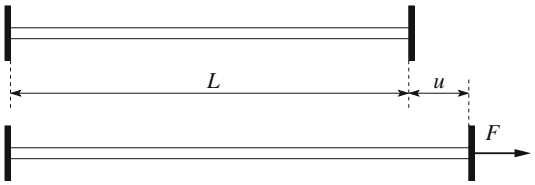

Fig. 4 A one-dimensional bar of length L stretched by a displacement u applied at the right support

hardening. After the onset of softening, the stress decreases and remains uniform, but the strain can become nonuniform. An arbitrarily small imperfection (e.g. reduction of the strength of one element) triggers localization of the inelastic processes into the weakest element while the other elements enter the unloading regime. For a given change of stress, the corresponding changes of elastic strain and of inelastic strain are uniquely determined by the constitutive law. The change of the total bar elongation is the integral of the strain change, and the contribution of the elastic strain change that takes place in all the elements is independent of the number of elements but the contribution of the inelastic strain change that takes place in one single element is proportional to the element size and thus inversely proportional to the number of elements (assuming a uniform mesh). With mesh refinement, the slope of the post-peak part of the load-displacement diagram becomes steeper and the structural response is thus more brittle. In the limit for the number of elements approaching infinity, the size of the softening element tends to zero and the dissipation rate as well. A regularization technique is required to prevent localization of inelastic processes into an arbitrarily small volume and to enforce the correct dissipation rate and correct slope of the load-displacement diagram.

The regularization of the solution requires the introduction of an additional scalar parameter with the dimension of length, related to the thickness of the localization band. Similar to Grassl and Jirásek (2006b), the current model is regularized by integral-type nonlocal averaging of the cumulated plastic strain κ. The value of the nonlocal cumulated plastic strain, $\bar{\kappa}$, depends on the surrounding points that are within a certain distance R, related to the internal length of the model, i.e., to the size and spacing of the dominating heterogeneities in the microstructure.

It turns out that simply computing damage from the nonlocal cumulated plastic strain $\bar{\kappa}$ provides only a partial regularization. The dissipation rate remains finite but plastic yielding still localizes into one single element; see Grassl and Jirásek (2006b). Full regularization can be achieved if damage $D(\hat{\kappa})$ is computed from an internal variable

$$\hat{\kappa} = (1-m)\kappa + m\bar{\kappa} \tag{63}$$

defined as a linear combination of the local and nonlocal cumulated plastic strains, with dimensionless parameter m larger than 1. This strategy has been shown to act as a proper localization limiter (preventing localization into a band of zero thickness), to be free of stress locking, and to be computationally efficient since the plasticity problem remains local.

The nonlocal value of cumulated plastic strain is defined as

$$\bar{\kappa}(\mathbf{x}) = \int_V \alpha(\mathbf{x},\mathbf{s})\kappa(\mathbf{s})\mathrm{d}\mathbf{s} \tag{64}$$

where V is the spatial domain occupied by the bone, $\mathbf{x}$ is the point at which the nonlocal cumulated plastic strain is evaluated, $\mathbf{s}$ sweeps through the domain V, and

$$\alpha(\mathbf{x},\mathbf{s}) = \frac{\alpha_0(\parallel \mathbf{x}-\mathbf{s} \parallel)}{\int_V \alpha_0(\parallel \mathbf{x}-\mathbf{t} \parallel)\mathrm{d}\mathbf{t}} \tag{65}$$

is the nonlocal weight function, typically nonnegative and decaying with increasing distance $r = \parallel \mathbf{x}-\mathbf{s} \parallel$ between points $\mathbf{x}$ and $\mathbf{s}$. Function α_0 is selected here as the truncated quartic polynomial

$$\alpha_0(r) = \begin{cases} \left(1-\frac{r^2}{R^2}\right)^2 & \text{if } r < R \\ 0 & \text{if } r \geq R \end{cases} \tag{66}$$

Parameter R, called the nonlocal interaction radius, has the dimension of length and directly affects the size of the localization band.

Note that the nonlocal cumulated plastic strain affects only the damage evolution, while the current effective yield stress is computed from the local cumulated plastic strain. Therefore, the plastic stress-return algorithm is not affected by the nonlocal formulation and can be used in its standard form. After the evaluation of plastic strain increments in all Gauss points of the finite element model, the local values of κ are known and the nonlocal values $\bar{\kappa}$ can be obtained in a straightforward manner, approximating the integral in (64) by a finite sum.

The plastic dissipation rate $\mathscr{D}_p$ is given by the same expression (18) as for the local model, only with $D(\kappa)$ replaced by $D(\hat{\kappa})$, and it is thus guaranteed to remain nonnegative. To verify thermodynamic consistency, it is sufficient to show that the damage dissipation

$$\mathscr{D}_D = \tfrac{1}{2}(\mathbf{E}-\mathbf{E}^p):\mathbb{S}(\mathbf{E}-\mathbf{E}^p)\dot{D} \tag{67}$$

remains nonnegative. For a positive definite elastic stiffness $\mathbb{S}$, condition $\mathscr{D}_D \geq 0$ is satisfied if $\dot{D} \geq 0$, i.e., if damage cannot decrease. For the local model, D is a nondecreasing function of the local cumulated plastic strain κ, and the rate of κ is nonnegative. The rate of the local cumulated plastic strain is always nonnegative and this property is preserved by nonlocal averaging, provided that the nonlocal weight function is nonnegative, too. So the monotonicity of damage evolution would be automatically guaranteed for a model with damage

driven by the nonlocal cumulated plastic strain $\bar{\kappa}$. However, with $m > 1$, the combined nonlocal variable $\hat{\kappa}$ defined in (63) can decrease if the local cumulated plastic strain grows much faster than the nonlocal one. Therefore, to make sure that the model remains thermodynamically consistent, $\hat{\kappa}$ is considered as the maximum value of $(1-m)\kappa + m\bar{\kappa}$ over the previous history. This could be formalized by introducing another loading function and the corresponding complementarity conditions.

6 Numerical examples

This section first presents examples with homogeneous material properties that illustrate the main features of the proposed law, its proper implementation, and, using the nonlocal formulation, the convergence of the solution with mesh refinement. Then, an example of application to compression of vertebral bodies with heterogeneous material properties is presented.

6.1 Specimen with homogeneous properties

At first, the behavior of the local formulation is illustrated by a simulation of a single cubic element of edge length 1 mm. Afterward, a comparison between the local and nonlocal formulation is presented to illustrate the impact of the nonlocality on the solution.

In order to select reasonable parameters, the elasticity tensor and yield criterion were first taken from Matsuura et al. (2008), Zysset (2003), and Rincón-Kohli and Zysset (2009) and then, together with the hardening and softening parameters, were adjusted to match an experimental curve (Fig. 5). This approach to parameter selection is appropriate for the present examples, as their only purpose is to illustrate the characteristics of the material model. The parameters used, except if mentioned otherwise, are those listed in Table 1.

6.1.1 Local formulation

The experimental curve in Fig. 5 shows the typical behavior observed in compression of trabecular bone. Beyond a certain threshold, the bone accumulates irreversible strain and its stiffness is reduced, which in mechanical terms correspond to plasticity and damage, both considered in the current law. After reaching the ultimate point, the force gradually decreases.

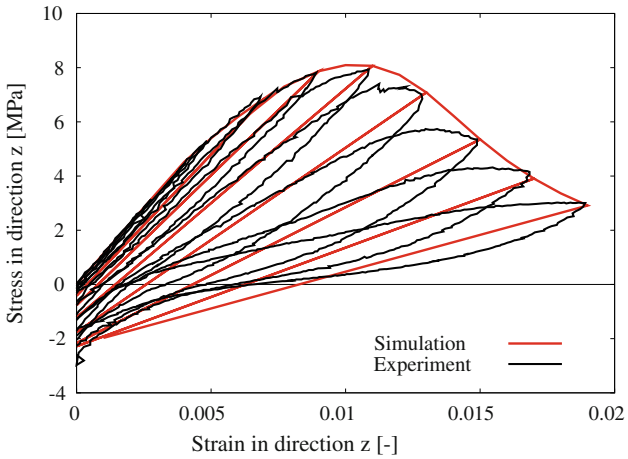

Fig. 5 Figure depicting a post-yield cyclic compressive test on a trabecular bone biopsy that shows the accumulation of irreversible strain. Parameters used are $\rho = 0.34$, $m_1 = m_2 = 0.8$ and $m_3 = 1.4$ (transversal isotropy)

The local formulation of the law has been implemented into OOFEM, an open-source object-oriented finite element code (Patzák and Bittnar 2001). All elements of the elasticity and yield tensors have been verified by simulating confined compression, tension and shear in several directions using a single cubic linear element of length 1 mm on which nodal displacements are imposed. The main results are presented in Fig. 6.

6.1.2 Nonlocal formulation

The nonlocal formulation has been introduced to ensure convergence of the localized solution upon mesh refinement. A bar of length 1 mm and cross-sectional area 0.2 mm × 0.2 mm has been discretized with different numbers of elements and subjected to confined compression up to 10% strain. To trigger localization, the yield stress of the central element has been reduced by 2%. Results obtained with both nonlocal and local formulations are presented in Figs. 7 and 8. By redistributing the damage from the weakest element to its neighbors, the nonlocal formulation prevents localization in a single element. Softening, which is directly linked to the damage parameter, occurs in all elements within a band of

Table 1 Default parameters used in the simulations (except if mentioned otherwise)

ε_0 [MPa]	ν_0	k	l	σ_0 [MPa]	χ_0	p	q	σ^H	s	D_C	a	R [mm]	m
2080	0.18	1.45	1.3	8.15	0.327	1.45	1.16	1.7	1100	0.925	200	0.25	1.5

The shear values are set to $\mu_0 = \frac{\varepsilon_0}{2(1+\nu_0)}$ and $\tau_0 = \frac{\sigma_0^{\pm}}{\sqrt{2(1+\chi_0^{\pm})}}$ and the yield criterion is considered as symmetric in tension and compression ($\sigma_0 = \sigma_0^+ = \sigma_0^-$ and $\chi_0 = \chi_0^+ = \chi_0^-$). Parameters R and m are relevant to nonlocal simulations only

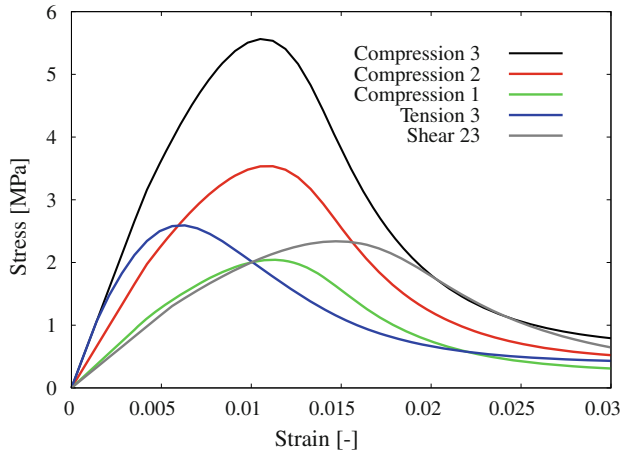

Fig. 6 Comparison of different loading cases. An orthotropic symmetry was used with $m_1 = 0.8, m_2 = 1$ and $m_3 = 1.2$, and the asymmetry between compression and tension was considered with $\sigma_0^+ = 0.6\sigma_0^-$ and $\chi_0^+ = (\chi_0^- + 1)\frac{(\sigma_0^+)^2}{(\sigma_0^-)^2} - 1$

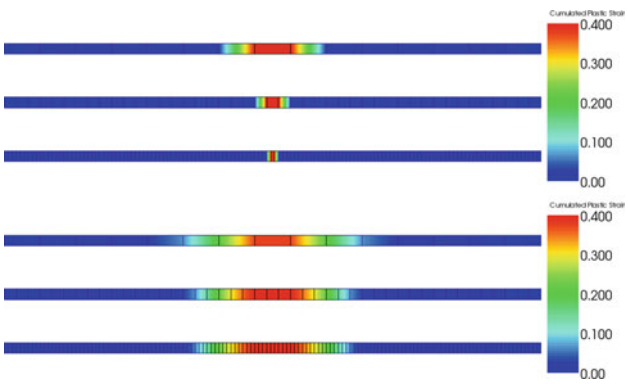

Fig. 7 A compressive displacement has been applied on a bar discretized by an increasing number of elements (from 15 to 135), using both nonlocal (*top*) and local (*bottom*) formulations. The figures depict the accumulation of plastic strain. While the nonlocal formulation clearly approaches a converged solution with mesh refinement, the local formulation highly depends on the mesh size as only the central element accumulates plastic strain. The hardening-softening parameters have been reduced to $s = 10$ and $a = 110$ for the nonlocal formulation and to $s = 2$ and $a = 110$ for the local formulation in order to clearly illustrate the impact of mesh size on the solution

width $2R$, which makes the solution independent of meshing (the mesh size needs to be smaller than the radius of interaction). Also the nonlocal parameters, R and m, have an impact on the stress-strain diagram. Reducing their value increases the slope of the softening while ultimate stress and residual stress at large strain are unaffected. For example, the strain corresponding to half the ultimate stress changes by 12.1% and −11.6% with a variation of ±10% of both R and m. These results are again independent of the meshing. The local formulation without any localization limiter leads to strain localization in a single element, as expected.

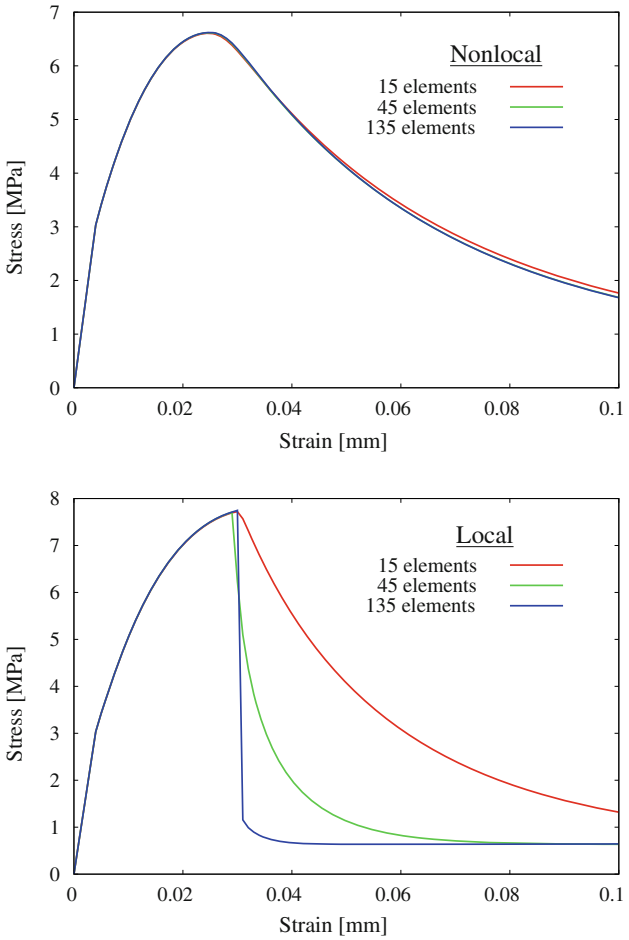

Fig. 8 Figure depicting the stress-strain diagram of the long bars presented in Fig. 7. As expected, the results of the nonlocal formulation are insensitive to the mesh size while for the local formulation the softening part strongly depends on the mesh size

6.2 Example of application

The nonlocal constitutive law has been applied to vertebral bodies. The finite element models of the vertebral bodies are identical to the models in Chevalier et al. (2008a), but the constitutive law is different and covers softening.

For the present model, the nonlocal tangent stiffness matrix has not been developed yet, and therefore the equilibrium iteration is performed with the secant stiffness, $\mathbb{S}_a^D = (1 - D)\mathbb{S}$, which provides a linear convergence rate.

6.2.1 Method

Vertebral bodies have been scanned using a high-resolution peripheral QCT (pQCT) system (XtremCT, 82 µm isotropic, 59.4 kV, 1000 µA, Scanco MedicalAG, Zürich, Switzerland) and the image data sets have been resampled to a resolution of 1312 µm. Bone voxels grey values have been converted to bone volume fractions using a calibration curve

Table 2 Description of the parameters used in the simulation of the vertebrae

ε_0 [MPa]	ν_0	k	l	σ_0^+ [MPa]	σ_0^- [MPa]	χ_0^+	χ_0^-	p	q	σ^H	s	D_C	a	R [mm]	m
8237.1	0.18	2.5	1.88	57.4	132.4	−0.748	0.340	2.5	0.86	6.0	37.5	0.6	22.5	3.936	1.5

The shear values are set equal to $\mu_0 = \frac{\varepsilon_0}{2(1+\nu_0)}$ and $\tau_0 = \frac{\sigma_0^{\pm}}{\sqrt{2(1+\chi_0^{\pm})}}$. Parameters R and m are only active in nonlocal simulations

Table 3 Quantitative results for the vertebral bodies

	Stiffness [N/mm]	Strength [N]	Ult. Displ. [mm]
B-L3	8459	5165	1.12
C-L4	14355	9488	1.23

based on hydroxyapatite content, and a threshold value has been chosen to define the external contours of the vertebrae. Voxels representing PMMA end plates (linear elastic and isotropic) have been added using an automated method and all the voxels have been converted to hexahedral elements. A more complete description of the method can be found in Chevalier et al. (2008a).

Simulations are performed under compression along the anatomic superior-inferior axis. The parameters have been chosen using a similar approach as for the homogeneous models. The parameters for the elasticity tensor and yield criterion have been first taken from the study of Chevalier et al. (2008a). Then, together with the hardening and softening parameters, they have been adjusted to match the ultimate force of the simulation presented in Chevalier et al. (2008a) and to give a reasonable softening when compared to the experiments presented in Chevalier et al. (2008b) (Table 2). The end plates are described by a linear elastic and isotropic constitutive law with Young's modulus of 3 GPa and Poisson's ratio of 0.35. Since large deformations arise due to localization, the Jacobian is evaluated at every integration point in order to detect negative volumes. The last step considered in the simulation is the last step without a negative Jacobian. Of course, a more rigorous approach would be to use a large-strain formulation with an additional term that reflects the re-hardening of the material after pore closure. This is the subject of further research.

6.2.2 Results

The force-displacement curve exhibits the expected behavior, reaching an ultimate point after which softening occurs (Fig. 9). The vertebra C-L4 presents a higher stiffness and peak force, with respective values of 14.4 GPa and 9.49 kN, than specimen B-L3, with respective values of 8.46 GPa and 5.16 kN. The ultimate displacement for both specimens is similar with values of 1.23 and 1.12 mm for specimens C-L4 and B-L3, respectively (Table 3).

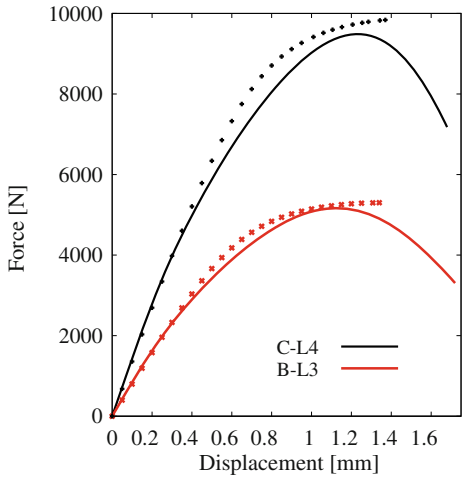

Fig. 9 Force-displacement curves from the simulation made on the two vertebral bodies (*continuous lines*). *Dotted lines* are the simulation results found in Chevalier et al. (2008a)

Within the vertebral body, the inelastic processes (irreversible strain and damaging) concentrate in specific regions in each specimen (Fig. 10). Before the ultimate point, these regions are similar to the result of Chevalier et al. (2008c), who used a nonlinear constitutive law without softening. Within sample B-L3, the inelastic process clearly evolves in two distinct layers, while in sample C-L4 it is more diffuse. After the ultimate point, the inelastic process localizes mostly into a single layer for each vertebra so that only one region over the height of the sample accumulates strain.

7 Conclusion

A novel constitutive relation has been presented; it captures the hardening–softening response of trabecular bone in compression. The model couples damage and plasticity and is enhanced with a nonlocal formulation which ensures mesh independence of the solution (Hansen and Schreyer 1994; Lubarda and Krajcinovic 1995; Maugin 1992; Zysset and Curnier 1996; Grassl and Jirásek 2006b). The constitutive law has been implemented in a finite element package, and numerical examples have been presented to show the potential of the approach.

The constitutive law has been developed primarily for numerical simulations performed under compression. While

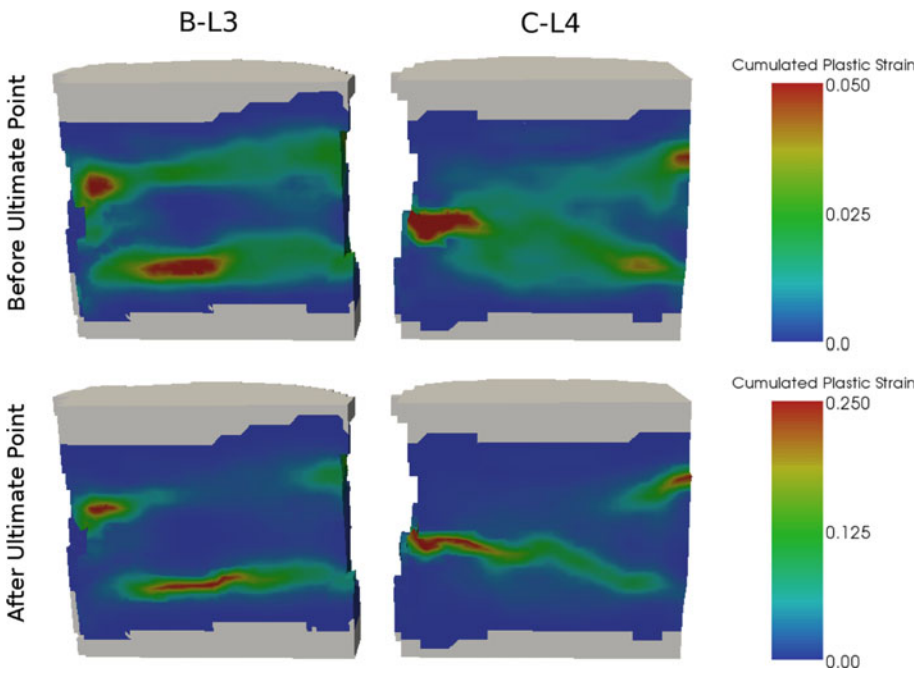

Fig. 10 Lateral cut of the vertebral bodies showing the cumulated plastic strain before and after the ultimate point for both vertebrae. Note that the scales in the *top* and *bottom* figures are different

it includes an asymmetric tension/compression yield function, the critical damage D_C is a scalar and is active for all strain states. Therefore, a critical damage value lower than 1 prevents the stress from completely vanishing, even in tension. This choice is motivated by applications that mainly require an accurate description of the mechanical behavior of bone in compression. For example, FE simulations of vertebral bodies are usually performed under compression or bending (Crawford et al. 2003; Chevalier et al. 2008a,b; Eswaran et al. 2006, 2007) and distal radius fractures are investigated using FE simulations performed under compression (Pistoia et al. 2002; Boutroy et al. 2008; Melton et al. 2007; Macneil and Boyd 2008; Verhulp et al. 2008). As these two anatomical sites are of high importance in fractures related to osteoporosis, we believe that describing the compressive behavior of trabecular bone is highly relevant.

The development of this constitutive law is motivated by advances in numerical methods that provide a patient-specific digital model of bone directly from clinical tomography using an automated procedure (Chevalier et al. 2008a,b; Pahr and Zysset 2009). To show the compatibility of the proposed constitutive law with these numerical methods, the law has been adopted by voxel models created from vertebral bodies using the method presented in Chevalier et al. (2008a). On the one hand, the resulting force-displacement curve shows the desired softening behavior, which is the novel feature of the law. On the other hand, interesting conclusions can be made by looking at the regions where inelastic processes (irreversible strain and damage accumulation) occur within the vertebral body. First, similar to Chevalier et al. (2008c), several transverse layers can be observed before the ultimate point, whereas beyond this point, results start to differ. The nonlinear constitutive law in Chevalier et al. (2008c) does not include softening and the layers are simply growing while the current voxel model presents, beyond the ultimate force, a single layer of localized inelastic processes (Fig. 10). The explanation is that the solution with several layers becomes unstable and the numerical solution is attracted by the stable solution with dissipative processes localized into a single layer (Bažant and Cedolin 1991). The effect of softening on the size of the region where plastic yielding and damage growth occur is of high importance for simulations reaching moderate strains, because the total energy dissipation during failure can be properly evaluated only when this effect is taken into account.

Finally, several steps are required before using the proposed models directly in studies focused on clinical applications (e.g. Keaveny et al. 2007; Imai et al. 2009). First, there is a need for identification of a set of parameters suitable for trabecular bone. In the literature, data for elasticity and yield criterion are already available (Matsuura et al. 2008; Rincón-Kohli and Zysset 2009; Chevalier et al. 2008a), while the hardening and softening parameters remain to be determined and thus require an experimental study. Second, using the secant stiffness to solve the global problem provides only linear convergence rate. In applications reaching moderate strains, it would be preferable to use a different strategy to reduce the computational time, for example by developing a nonlocal tangent stiffness (Jirásek and Patzák 2002). With these issues addressed, we believe the proposed law to be highly attractive for bone mechanics applications based on continuum FE models.

Acknowledgments This research was part of project 05-Z26 entitled "A nonlocal damage model for trabecular bone", supported by the AO Research Fund of the AO Foundation, and of project 106/08/1508 entitled "Regularized model for localized compressive failure of trabecular bone", supported by the Czech Science Foundation. The authors would like to thank Prof. Bořek Patzák of the Czech Technical University in Prague for kind assistance with his object-oriented finite element code, OOFEM.

References

Bažant ZP, Cedolin L (1991) Stability of structures. Oxford University Press, New York and Oxford

Bažant ZP, Jirásek M (2002) Nonlocal integral formulations of plasticity and damage: survey of progress. J Eng Mech ASCE 128: 1119–1149

Boutroy S, Van Rietbergen B, Sornay-Rendu E, Munoz F, Bouxsein ML, Delmas PD (2008) Finite element analysis based on in vivo hr-pqct images of the distal radius is associated with wrist fracture in postmenopausal women. J Bone Miner Res 23(3):392–399

Chevalier Y, Charlebois M, Pahr D, Varga P, Heini P, Schneider E, Zysset P (2008a) A patient-specific finite element methodology to predict damage accumulation in vertebral bodies under axial compression, sagittal flexion and combined loads. Comput Methods Biomech Biomed Eng 11(5):477–487

Chevalier Y, Pahr D, Charlebois M, Heini P, Schneider E, Zysset P (2008b) Cement distribution, volume, and compliance in vertebroplasty: some answers from an anatomy-based nonlinear finite element study. Spine 33(16):1722–1730

Chevalier Y, Pahr DH, Zysset PK (2008c) Anatomy and morphology-based smooth finite element models of human vertebral bodies. In: 16th Annual symposium on computational methods in orthopaedic biomechanics, San Francisco, California, March 1st, 2008

Crawford RP, Cann CE, Keaveny TM (2003) Finite element models predict in vitro vertebral body compressive strength better than quantitative computed tomography. Bone 33(4):744–750

Cristofolini L, Juszczyk M, Martelli S, Taddei F, Viceconti M (2007) In vitro replication of spontaneous fractures of the proximal human femur. J Biomech 40(13):2837–2845

Curnier A, He Q-C, Zysset P (1995) Conewise linear elastic materials. J Elast 37(1):1–38

Eswaran SK, Gupta A, Adams MF, Keaveny TM (2006) Cortical and trabecular load sharing in the human vertebral body. J Bone Miner Res 21(2):307–314

Eswaran SK, Gupta A, Keaveny TM (2007) Locations of bone tissue at high risk of initial failure during compressive loading of the human vertebral body. Bone 41(4):733–739

Fondrk MT, Bahniuk EH, Davy DT (1999a) A damage model for nonlinear tensile behavior of cortical bone. J Biomech Eng 121(5):533–541

Fondrk MT, Bahniuk EH, Davy DT (1999b) Inelastic strain accumulation in cortical bone during rapid transient tensile loading. J Biomech Eng 121(6):616–621

Garcia D, Zysset P, Charlebois M, Curnier A (2009) A three-dimensional elastic plastic damage constitutive law for bone tissue. Biomech Model Mechanobiol 8:149–165

Gibson LJ, Ashby MF (1999) Cellular solids: structure and properties. 2. Cambridge University Press, Cambridge

Grassl P, Jirásek M (2006a) Damage-plastic model for concrete failure. Int J Solids Struct 43(22–23):7166–7196

Grassl P, Jirásek M (2006b) Plastic model with non-local damage applied to concrete. Int J Numer Anal Methods Geomech 30(1): 71–90

Green AE, Naghdi PM (1965) A general theory of an elastic-plastic continuum. Springer, Berlin

Hansen NR, Schreyer HL (1994) A thermodynamically consistent framework for theories of elastoplasticity coupled with damage. Int J Solids Struct 33(3):359–389

Hayes WC, Carter DR (1976) Postyield behavior of subchondral trabecular bone. J Biomed Mater Res 10(4):537–544

Imai K, Ohnishi I, Matsumoto T, Yamamoto S, Nakamura K (2009) Assessment of vertebral fracture risk and therapeutic effects of alendronate in postmenopausal women using a quantitative computed tomography-based nonlinear finite element method. Osteoporos Int 20(5):801–810

Jirásek M, Patzák B (2002) Consistent tangent stiffness for nonlocal damage models. Comput Struct 80(14–15):1279–1293

Kachanov LM (1986) Introduction to continuum damage mechanics. Springer, Berlin

Keaveny TM, Donley DW, Hoffmann PF, Mitlak BH, Glass EV, San Martin JA (2007) Effects of teriparatide and alendronate on vertebral strength as assessed by finite element modeling of qct scans in women with osteoporosis. J Bone Miner Res 22(1):149–157

Keaveny TM, Morgan EF, Niebur GL, Yeh OC (2001) Biomechanics of trabecular bone. Annu Rev Biomed Eng 3:307–333

Lemaitre J, Chaboche J-L (1994) Mechanics of solid materials. Cambridge University Press, Cambridge

Lubarda VA, Krajcinovic D (1995) Some fundamental issues in rate theory of damage-elastoplasticity. Int J Plas 11(7):763–797

Macneil JA, Boyd SK (2008) Bone strength at the distal radius can be estimated from high-resolution peripheral quantitative computed tomography and the finite element method. Bone 42(6): 1203–1213

Matsuura M, Eckstein F, Lochmüller E-M, Zysset PK (2008) The role of fabric in the quasi-static compressive mechanical properties of human trabecular bone from various anatomical locations. Biomech Model Mechanobiol 7(1):27–42

Maugin GA (1992) The Thermomechanics of plasticity and fracture. Cambridge University Press, Cambridge

Melton LJ, Riggs BL, van Lenthe GH, Achenbach SJ, Müller R, Bouxsein ML, Amin S, Atkinson EJ, Khosla S (2007) Contribution of in vivo structural measurements and load/strength ratios to the determination of forearm fracture risk in postmenopausal women. J Bone Miner Res 22(9):1442–1448

Natali AN, Carniel EL, Pavan PG (2008a) Constitutive modelling of inelastic behaviour of cortical bone. Med Eng Phys 30(7): 905–912

Natali AN, Carniel EL, Pavan PG (2008b) Investigation of bone inelastic response in interaction phenomena with dental implants. Dent Mater 24(4):561–569

Pahr D, Zysset P (2009) From high-resolution ct data to finite element models: development of an integrated modular framework. Comput Methods Biomech Biomed Engin 12(1):45–57

Patzák B, Bittnar Z (2001) Design of object oriented finite element code. Adv Eng Softw 32(10–11):759–767

Pistoia W, van Rietbergen B, Lochmller E-M, Lill CA, Eckstein F, Regsegger P (2002) Estimation of distal radius failure load with micro-finite element analysis models based on three-dimensional peripheral quantitative computed tomography images. Bone 30(6):842–848

Prendergast P (1997) Finite element models in tissue mechanics and orthopaedic implant design. Clin Biomech 12(6):343–366

Rakotomanana L, Curnier A, Leyvraz F (1991) An objective anisotropic elastic plastic model and algorithm applicable to bone mechanics. Eur J Mech Solid 10(3):327–342

Rincón-Kohli L, Zysset P (2009) Multi-axial mechanical properties of human trabecular bone. Biomech Model Mechanobiol 8(3): 195–208

Simo JC, Hughes TJR (2000) Computational Inelasticity. Interdisciplinary Applied Mathematics. Springer, corrected edition

Simo JC, Taylor RL (1985) Consistent tangent operators for rate-independent elastoplasticity. Comput Methods Appl Mech Eng 48(1):101–118

Verhulp E, van Rietbergen B, Müller R, Huiskes R (2008) Indirect determination of trabecular bone effective tissue failure properties using micro-finite element simulations. J Biomech 41(7):1479–1485

Zysset P (1994) A constitutive law for trabecular bone. PhD thesis, EPFL, Lausanne

Zysset P, Curnier A (1995) An alternative model for anisotropic elasticity based on fabric tensors. Mech Mater 21(4):243–250

Zysset PK, Curnier A (1996) A 3d damage model for trabecular bone based on fabric tensors. J Biomech 29(12):1549–1558

Zysset P, Rincón L (2006) Mechanics of biological tissue., Chapter an alternative fabric-based yield and failure criterion for trabecular bone. Springer, Berlin, pp 457–470

Zysset PK (2003) A review of morphology-elasticity relationships in human trabecular bone: theories and experiments. J Biomech 36(10):1469–1485